Spectral mapping of thermal conductivity through nanoscale ballistic transport

Yongjie Hu, Lingping Zeng, Austin J. Minnich, Mildred S. Dresselhaus, Gang Chen

1. Modeling and simulation details.

The time-domain thermoreflectance (TDTR) experiments measure the transient thermoreflectance response of metallic heaters in the short time domain (0~6 ns), with sub-picosecond temporal resolution. Since the change in thermoreflectance is linearly proportional to the change in temperature, measuring thermoreflectance is equivalent to measuring the temperature of the metallic heaters [1]. To gain insight into the thermal transport in the experiments, we numerically solve the full spectral Boltzmann transport equation (BTE) under the relaxation time approximation and compare the BTE solution to the Fourier prediction to obtain the effective thermal conductivities across a wide range of length scales [2]. The simulation geometry consists of a periodic heater array sitting on top of the underlying substrate, mimicking the experimental sample configurations. Since the structure is periodic, the system can be studied by looking at the thermal transport in one single pitch of the repeated structure by applying periodic boundary conditions. Both the BTE and Fourier simulations are performed under transient heating conditions.

To solve the BTE, we used the recently developed variance-reduced Monte Carlo (VRMC) simulation technique [3-4] which substantially improves the computational efficiency and accuracy through the introduction of a reference state. In the VRMC model, only the deviation from the reference state is simulated. The deviational BTE is shown in Eq. (S1):

$$\frac{\partial e^*}{\partial t} + \overrightarrow{v_{\omega,p}} \cdot \nabla e^* = -\frac{e^* - e_0^*}{\tau_{\omega,\text{T}}} \tag{S1}$$

where $e^* = \hbar\omega(f_\omega - f_{\omega 0}^{eq})$ is the deviational phonon energy distribution, and $e_0^* = \hbar\omega(f_{\omega 0} - f_{\omega 0}^{eq})$ is the locally thermalized deviational energy distribution, $\hbar\omega$ is the phonon quantum of energy with $\hbar$ being the Planck constant divided by 2π, f_ω is the actual phonon distribution function, $f_{\omega 0}$ is the Bose-Einstein distribution function, and $v_{\omega,p}$ is the phonon group velocity. The reference distribution function $f_{\omega 0}^{eq}$ is the Bose-Einstein distribution function evaluated at a reference temperature T_{eq}.

For the heater, we assume phonons as the sole heat carriers and use the experimental dispersion relation along the [100] direction [5]. No electronic contribution to heat transport is considered. The phonon lifetime in the heater is assumed to be a constant, 10ps. For the silicon substrate, we use first principles density functional theory (DFT) calculated lifetimes and the experimentally measured phonon dispersion along the [100] direction as the input [5]. Both acoustic and optical

phonon branches are included in the simulation. The reference temperature in our simulations is chosen to be the substrate initial temperature (300 K), and thus no phonon is initialized in the substrate, since the deviational energy is zero. In the heater, we discretize the dispersion into 2000 frequency bins and randomly populate five million computational phonon particles at t = 0 s according to the phonon spectrum of the metal transducer. The initialized phonon particles are allowed to move subject to the specified boundary and interface conditions. Except for the four side surfaces of the substrate, for which periodic boundaries are assumed. All the other boundaries are approximated as diffuse adiabatic walls, consistent with experimental conditions, except at the heater-substrate interface, where phonons have a finite probability to either transmit through interface or reflect off it. The interface transmittance values are calculated using the model described in Ref. [6]. During each time step, we track the trajectory of each particle, and we determine whether boundary or interface scattering occurs by comparing the particle's position with the boundary and interface planes. If phonons reach one diffuse wall, they are diffusely reflected back into the domain; if phonons arrive at one periodic boundary, they are moved to the corresponding boundary. If interface scattering occurs, a random number is generated and compared with the relevant phonon's transmissivity to determine whether transmission or reflection occurs subsequently [7]. The heat flow into the substrate results from phonon transmission from the metal transducer to the substrate. At the end of each time step, we sample the phonon energy in each discretized spatial cell and we then invert the local phonon energy density to determine the equivalent equilibrium temperature distribution, as shown in Eq. (S2):

$$u = \sum_p \int_0^{\omega_{max,p}} \hbar\omega f_{\omega 0}^T D(\omega, p)\, d\omega \qquad (S2)$$

where u is the local phonon energy density, T is the equivalent equilibrium temperature to be computed, $\omega_{max,p}$ is the maximum phonon frequency for branch p, while $D(\omega, p)$ is the phonon density of states for branch p, and the summation is over all the phonon branches. Anharmonic scattering is processed as a probabilistic step following the energy sampling [7]. Anharmonic scattering, if it occurs, alters all the phonon properties (travelling direction, frequency, branch, and group velocity), expect for the phonon position. The 'advection – energy sampling – scattering' is repeated until the specified simulation time is reached. Over the course of the simulation, the heater surface temperature is recorded as a function of simulation time.

The interface conductance G is defined as the heat flux across an interface divided by the equivalent equilibrium temperature difference across that interface, and the interface conductance can be related to the spectral phonon transmissivity $T_{12}(\omega)$ by calculating the heat flux and the equivalent equilibrium temperature difference on each side of the interface [6, 8]:

$$G = q/\Delta T \qquad (S3)$$

$$q = \sum_p \int_0^{\omega_{max,p}} d\omega \int_0^{2\pi} d\phi \int_{-1}^{1} \mu\, d\mu \left\{ e^* v_{\omega,p} D(\omega, p) T_{12\omega} \right\} \qquad (S4)$$

where q is the heat flux at the interface, ΔT is the temperature difference across the interface, μ is the directional cosine, and ϕ is the azimuthal angle. Note that e^* depends upon the frequency, branch, and phonon propagation direction.

The substrate thermal conductivity is treated as a fitting parameter to match the Fourier solution to that of the phonon BTE. An example of the fitting result for a heater size of 600 nm is shown in Fig. S1. At a 600nm heater size, the effective substrate thermal conductivity, a measure of the degree of quasiballistic transport in the substrate, is much lower than the bulk value, indicating a significant ballistic effect.
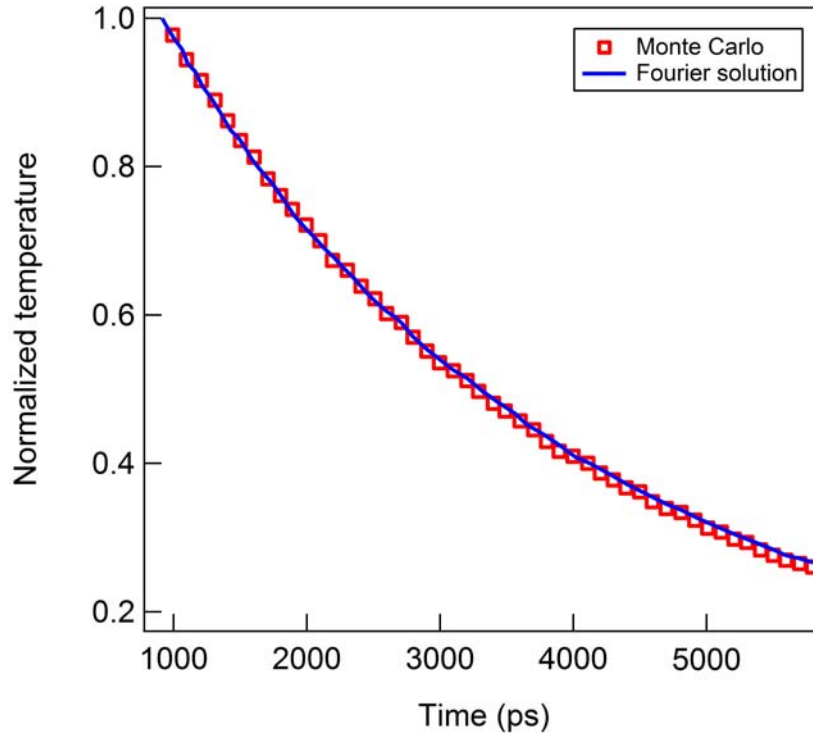
Supplementary Figure 1. Example of the fitting of the substrate effective thermal conductivity by matching the Fourier solution to the BTE results at a heater size of 600 nm, and a period of 1200 nm. The best fitting provides an effective thermal conductivity of k = 46 W/mK.

To solve the Fourier diffusion equation, we use the commercial software package: COMSOL Multiphysics (http://www.comsol.com). The initial, boundary, and interface conditions are consistent with those used in the VRMC model [3-4]. A thin layer thermal resistance between the metallic thermal transducer and the substrate materials is included, whose conductance (G) equals the interface conductance calculated from the interface transmissivities in the VRMC model. To improve the speed of the calculation involving different values of the substrate thermal conductivity k, we use a modified version of a standard multilayer model for analyzing TDTR signals [1]. In the typical model, the surface temperature for a multilayer stack consisting of the transducer, interface, and substrate subject to a Gaussian pump and probe beam is obtained using transfer matrices. To use this approach for dots, we first solve the heat equation in 3D Cartesian coordinates, rather than in cylindrical coordinates, since the geometry of the dot array is naturally represented in this coordinate system. We define the z direction as the cross-plane direction, while the x and y directions are the two in-plane directions. The surface temperature

3

frequency response to a periodic heating with frequency omega, H(ω), can be analytically represented as a function of the in-plane spatial frequencies, q_x and q_y, using the same equations as in Ref. [1]. The heating profile, X_{nm} of a square dot array, can be exactly expanded in a Fourier series as:

$$X_{nm} = \begin{cases} D^2/L^2, & n = m = 0 \\ \frac{D/L}{2\pi m j}(1 - \exp(-jm\Omega_0)), & n = 0, m \neq 0 \\ \frac{D/L}{2\pi n j}(1 - \exp(-jn\Omega_0)), & n \neq 0, m = 0 \\ \frac{-(1-\exp(-jm\Omega_0)(1-\exp(-jn\Omega_0))}{4\pi^2 nm}, & n \neq m \neq 0 \end{cases} \qquad (S5)$$

where X_{mn} denote the Fourier coefficients for a two-dimensional square wave, $\Omega_0 = 2pj/L$, j is the unit imaginary number, n and m correspond to the spatial frequencies $q_x = n\Omega_0$ and $q_y = m\Omega_0$, respectively, and D and L are the width and period of the dot array, respectively. Then, by performing the same sequence of steps in Ref [1], namely performing an inverse Fourier transform and averaging over the same spatial profile to model the probe sampling, the following expression for H(ω) is obtained:

$$H(\omega) = \sum_n \sum_m |X_{nm}|^2 \left(\frac{-E}{C}\right)_{n,m} \qquad (S6)$$

where E and C are the elements of the transfer matrices defined in prior works. This function can then be used directly to fit the experimental data as in Ref [1].

To account for the discontinuous nature of the dots, we model the transducer as a special layer in which the thermal conductivity in the in-plane directions is set to 0 while the cross-plane value remains its normal value. In this way, heat conduction in the transducer can only occur in the cross-plane direction, transferring the square wave heating profile in the transducer to the substrate.

This procedure neglects the Gaussian intensity variation of the pump and probe beams over the dot array. However, the heat conduction due to this pump intensity variation is much slower than heat conduction from the dots by a factor of $(D/P)^2$, where D is the dot width and P is the pump diameter. Since a P value of 60 ~ 100 microns is much larger than the typical dot widths considered in this work, the slower heat conduction over the length scales of the pump can be neglected with excellent accuracy. Note that the 60 micrometer heat size D is effectively defined by the pump diameter. To check whether the model is still valid at this extreme case, we performed additional calculations including the effects of Gaussian intensity variation of the pump and probe beams, as well as the periodicity of the multi-heater arrays, and we fitted the experimental data in this way. No appreciate difference in fitted results of thermal conductivity (k) has been observed.

4

We should also point out that the Fourier fitting to the experimental results provides good fittings when the heater size $D > 30$ nm, and becomes worse at $D = 30$ nm, as shown in Fig.S2. This is expected since the Fourier law cannot well capture the ballistic limit, where a very high portion of the phonons experience ballistic transport [9]. This poor fitting is not a major concern for the final extraction of the phonon MFP distributions, since the purpose is to use the effective thermal conductivity to extract the phonon MFP distributions, and the ballistic transport effect is thus properly included in the suppression function.

5
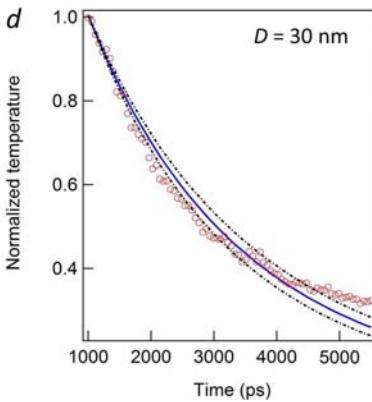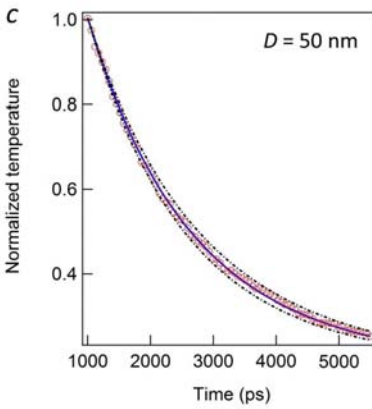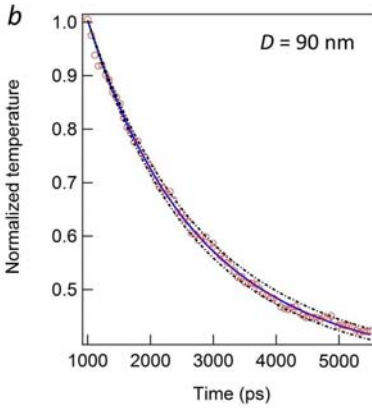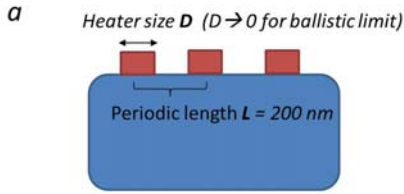
Supplementary Figure 2. Experiment designed to verify the transition of heat transfer into the ballistic limit. **a,** this schematic shows the fabrication strategy: the pitch size is fixed at 200 nm, and is relatively long to enhance the ballistic effect by avoiding mutual coupling from phonons injected from different heaters. Heaters of different sizes under 100 nm are fabricated. **b-d,** experimental data (red circle) is fit by the diffusive model (blue line) for 90 nm, 50 nm and 30 nm heater sizes, respectively. To illustrate the fitting sensitivity, calculated curves (black dots) using the thermal conductivity changed by ± 10% of the best value are plotted.

6

2. The structural and material design of nanoscale heaters

2.1 Nano-patterned periodic metallic heater array

The nanoscale heaters are two-dimensional arrays with a fixed filling fraction (FF, the ratio of the heater size (D) to the array period (L)) of 1:2. The samples are prepared using electron beam lithography and metal evaporations to define and insulate the heaters from surrounding patterns. Alignment with stitching accuracy down to sub-10 nm is applied to connect the two layers with nanoscale gaps for thermal insulation (Elionix ELS, 125 kV) [10]. High magnification SEM images of the small diameter (30 nm and 90 nm) samples are shown in Figure S3.
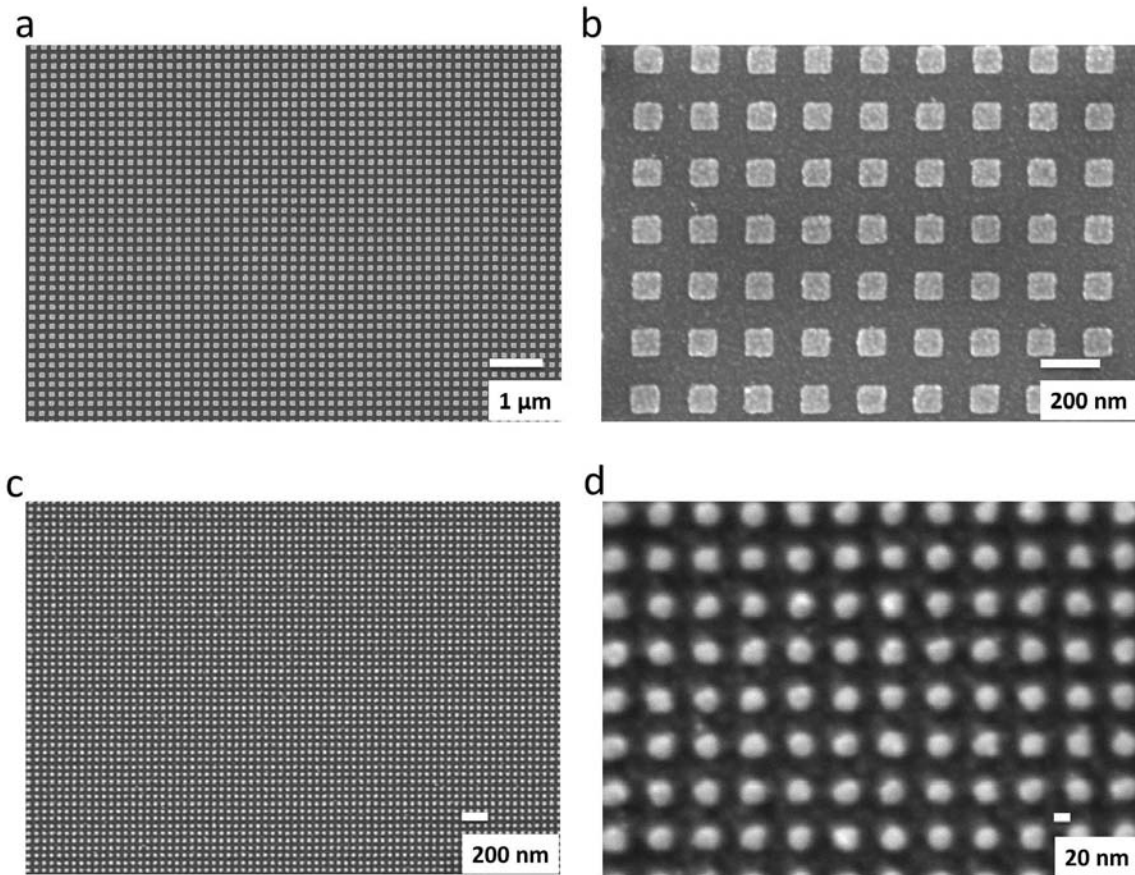
Supplementary Figure 3. SEM images of metallic patterns of small heater sizes. a) and b), 90 nm heater width. c) and d), 30 nm heater width.

2.2 Effect of pattern periodicity

Our experiments, calibrations, and simulations, all included the effects from periodic heater arrays and their mutual interactions. Our simulation used proper boundary conditions (periodic boundary condition) to take into account interactions among heaters. In addition, we expect the heat dissipation rate (and thereby the substrate effective thermal conductivity) in the heater

7

depends upon the design of the filling fraction, which is the ratio of the heater size (*D*) to the array period (*L*). We have performed such detailed simulations and discussions in Ref. 11.

As the distance between adjacent heaters becomes shorter than the phonon mean free path, additional size effects are introduced [11]. This effect is properly accounted for by the suppression function S(Λ/*D*, *D*/*L*), which is extracted by comparing experimental data and first-principles simulation results on Si, as explained in the manuscript. Since our experiments maintained the values of *D*/*L* approximately constant, S is only a function of Λ/*D*.

2.3 Effect of heater shape at small heater sizes

For our smallest heater size (30 nm), the metallic patterns look round shaped due to the resolution of lithography process, as shown in Fig. S3(d). To check whether the heater shape affects fitting results for the 30 nm heater width, we performed additional simulations with both square and circular shapes. The cross-sectional areas are kept equal for both heater shapes. As shown in Fig. S4, the temperature dependence curves from two different heater shapes overlap excellently, implying that the heater shape at ~ 30 nm heater size does not influence our interpretation significantly.
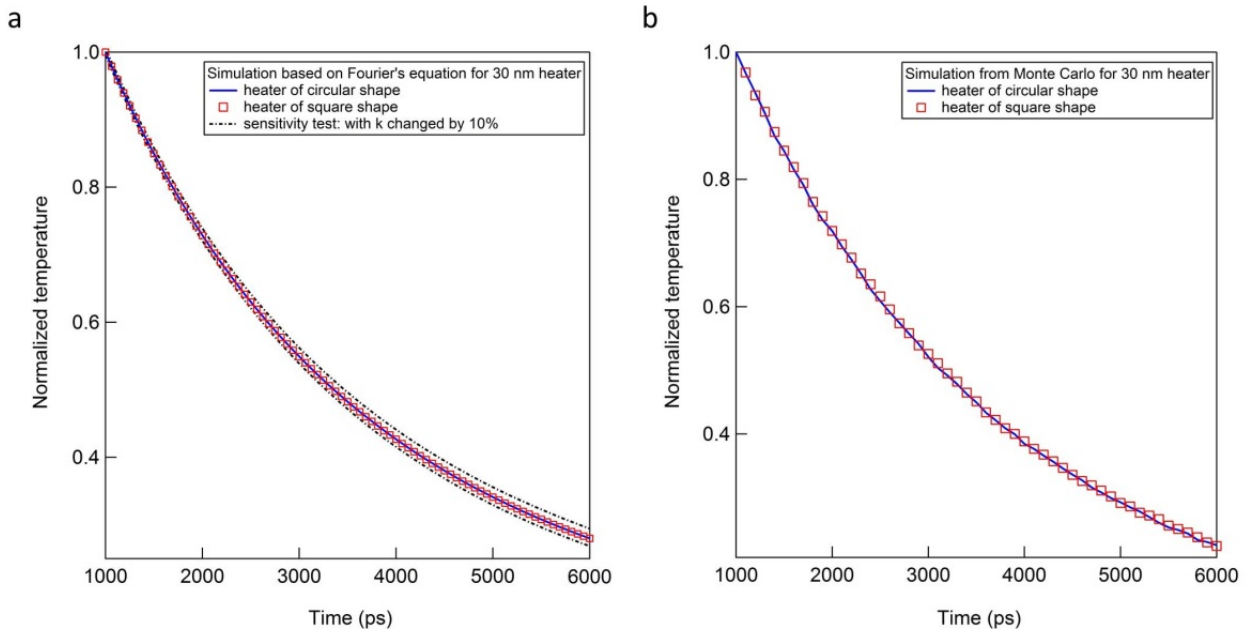
Supplementary Figure 4. Comparing temperature decay curves for 30 nm heaters with square shape (red square) and circular shape (blue line), respectively. a), simulations based on Fourier's equation. b), simulation from Monte Carlo modeling. Both simulations show no appreciable differences between square and circular heaters. For simulations based on Fourier's equation, we can intentionally change the thermal conductivity *k* by ± 10% (black dashed lines, results from square and circular shaper are totally overlapping) to test the sensitivity.

2.4 Effect of different heater materials

8

In theory, phonon transmission across an interface and the subsequently ballistic phonon transport is a coupled process [12]. It is hence uncertain whether the phonon MFP we extracted is influenced by the choice of the transducer that injects phonons into the substrate. We have tested Al and Cu as heater materials on sapphire, and found that the measured thermal conductivity reduction is similar in each case (Fig.S5).
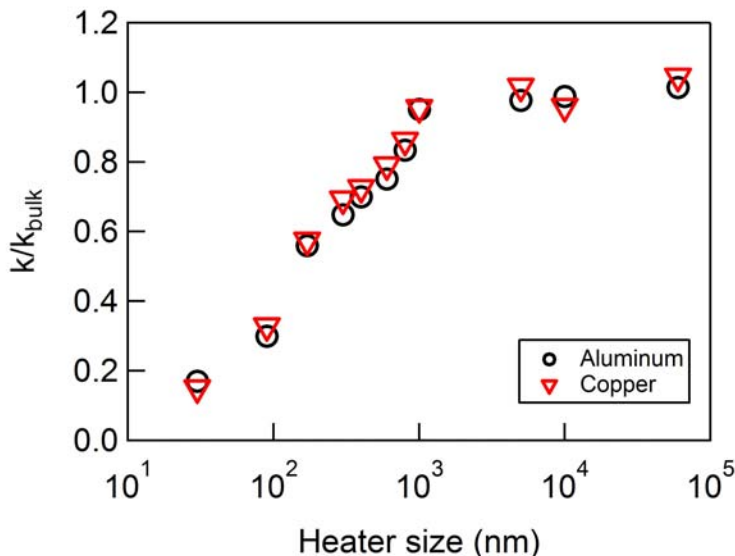
Supplementary Figure 5. Fitted thermal conductivity at different heater sizes at 300 K for a thermal transducer using aluminum (black circle) and copper (red triangle), with different interfacial transmissivity values between the two metals and substrate material (sapphire). No appreciable dependence of the thermal conductivity was observed for the different metal transducers.

2.5 Effect of the interface conductance

We also performed Monte Carlo simulations using different interface conductance values by varying the phonon transmittance on silicon, and we found that the simulation results do not change much (Fig.S6). These experiments and simulations show that ballistic phonon transport in the substrate is the dominant mechanism for the reduced thermal conductivity.

9
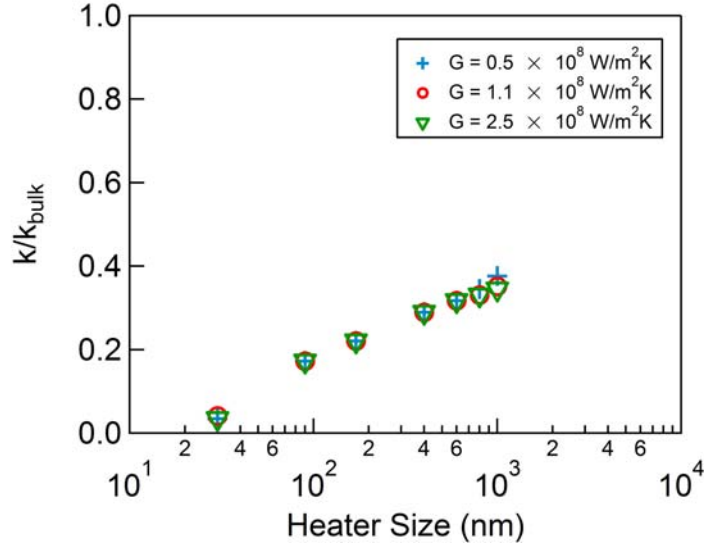
Supplementary Figure 6. Fitted thermal conductivity at different heater sizes for Si at 300 K for several specified values of interfacial conductance G, with each G corresponding to a different transmittance in the BTE/Monte Carlo model. There is no appreciable dependence of the thermal conductivity on the specified interfacial conductance. $G = 2.5 \times 10^8$, 1.1×10^8 and 5×10^7 W/m^{2}K for green triangles, red circles, and blue crosses, respectively.

2.6 Effect on the metal film quality

In order to measure the quality of metal film, we performed Van Der Paw measurements to determine the electrical conductivity of the film studied (Fig. S7). The obtained resistance values from eight different configurations are very close (~ 0.15 Ohm), indicating that the film is uniform and continuous.

The Van der Pauw Equation used in this analysis is:

$$\exp(-\pi R_A / R_S) + \exp(-\pi R_B / R_S) = 1, \tag{S7}$$

where $R_A = (R_{21,34} + R_{12,43} + R_{43,12} + R_{34,21})/4$, $R_B = (R_{32,41} + R_{23,14} + R_{14,23} + R_{41,32})/4$.

We obtain the resistivity of the silver film to be 34.7 nΩ·m, which is a couple of times more resistive than the literature value of bulk silver, and this higher resistivity is due to the polycrystalline nature of the film.

10

Supplementary Figure 7. Van Der Paw measurement. a, film geometry. b, illustration of the current injection and voltage measurements from different contact pairs. c, typical I-V curve. d, table of all eight groups of measurement results.

| Contact Sets:	R12,34 Current [A]	Voltage [V]	R34,12 Current [A]	Voltage [V]	R21,43 Current [A]	Voltage [V]	R43,21 Current [A]	Voltage [V]	R23,41 Current [A]	Voltage [V]	R41,23 Current [A]	Voltage [V]	R32,14 Current [A]	Voltage [V]	R14,32 Current [A]	Voltage [V]
	1.20E-11	1.47E-09	1.19E-11	-7.19E-10	1.48E-11	-8.89E-10	1.25E-11	-9.20E-10	1.06E-11	-1.65E-09	1.10E-11	-1.38E-09	9.63E-12	-9.31E-10	1.03E-11	2.78E-09
	2.91E-11	1.27E-09	3.73E-11	9.14E-10	6.98E-11	-4.17E-10	3.61E-11	-4.94E-10	3.92E-11	-1.56E-09	3.11E-11	-2.98E-09	2.76E-11	1.17E-09	2.95E-11	2.29E-09
	1.09E-10	-2.01E-09	8.04E-11	-6.29E-10	9.37E-11	1.44E-09	9.64E-11	3.34E-09	9.89E-11	-1.78E-09	1.03E-10	-2.19E-10	1.22E-10	8.91E-10	9.35E-11	-8.93E-10
	3.49E-10	2.10E-09	8.68E-10	-3.73E-10	2.67E-10	7.20E-10	3.54E-10	1.66E-09	2.90E-10	-2.09E-09	3.00E-10	1.82E-09	3.35E-10	-1.39E-09	2.57E-10	-9.88E-10
	-1.67E-10	-5.00E-11	9.70E-10	-2.69E-09	1.29E-09	-1.75E-09	1.09E-09	-5.96E-10	9.11E-10	1.30E-09	1.05E-09	-1.30E-10	7.80E-10	-1.30E-10	1.35E-09	9.11E-10
	3.61E-09	1.23E-09	3.22E-09	-1.65E-09	3.10E-09	-2.06E-09	3.74E-09	-1.42E-09	3.06E-09	-9.59E-10	2.87E-09	-1.06E-09	3.39E-09	-1.68E-09	2.84E-09	-1.92E-09
	1.06E-08	-2.19E-09	9.49E-09	-1.58E-09	1.04E-08	-2.76E-09	9.78E-09	-3.06E-09	1.02E-08	-3.45E-09	9.62E-09	-1.72E-09	9.59E-09	-5.24E-09	1.08E-08	-1.67E-09
	3.15E-08	-8.70E-09	3.07E-08	-6.92E-09	3.06E-08	-5.70E-09	3.20E-08	-5.70E-09	3.07E-08	-7.97E-09	3.16E-08	-7.98E-09	3.09E-08	-8.12E-09	3.12E-08	-1.00E-08
	9.91E-08	-2.59E-08	9.90E-08	-2.38E-08	1.01E-07	-2.07E-08	1.00E-07	-2.48E-08	9.91E-08	-2.53E-08	9.90E-08	-2.30E-08	1.00E-07	-2.31E-08	9.91E-08	-2.37E-08
	3.15E-07	-7.50E-08	3.16E-07	-7.42E-08	3.14E-07	-7.44E-08	3.15E-07	-7.42E-08	3.16E-07	-7.36E-08	3.15E-07	-7.21E-08	3.16E-07	-7.25E-08	3.15E-07	-7.44E-08
	9.97E-07	-1.63E-07	9.96E-07	-1.62E-07	9.97E-07	-1.61E-07	9.94E-07	-1.60E-07	9.96E-07	-1.57E-07	9.96E-07	-1.60E-07	9.93E-07	-1.58E-07	9.96E-07	-1.61E-07
	3.15E-06	-5.18E-07	3.15E-06	-5.14E-07	3.15E-06	-5.10E-07	3.15E-06	-5.11E-07	3.15E-06	-5.03E-07	3.15E-06	-5.01E-07	3.15E-06	-5.04E-07	3.15E-06	-5.08E-07
	9.96E-06	-1.66E-06	9.96E-06	-1.65E-06	9.96E-06	-1.62E-06	9.96E-06	-1.63E-06	9.96E-06	-1.60E-06	9.96E-06	-1.60E-06	9.96E-06	-1.62E-06	9.96E-06	-1.62E-06
	3.15E-05	-5.22E-06	3.15E-05	-5.22E-06	3.15E-05	-5.16E-06	3.15E-05	-5.19E-06	3.15E-05	-5.10E-06	3.15E-05	-5.08E-06	3.15E-05	-5.15E-06	3.15E-05	-5.16E-06
	9.96E-05	-1.57E-05	9.96E-05	-1.57E-05	9.96E-05	-1.58E-05	9.96E-05	-1.57E-05	9.96E-05	-1.55E-05	9.96E-05	-1.54E-05	9.96E-05	-1.54E-05	9.96E-05	-1.54E-05
	3.15E-04	-4.64E-05	3.15E-04	-4.64E-05	3.15E-04	-4.65E-05	3.15E-04	-4.64E-05	3.15E-04	-4.55E-05	3.15E-04	-4.56E-05	3.15E-04	-4.55E-05	3.15E-04	-4.54E-05
	9.96E-04	-1.54E-04	9.96E-04	-1.54E-04	9.96E-04	-1.54E-04	9.96E-04	-1.54E-04	9.96E-04	-1.52E-04	9.96E-04	-1.52E-04	9.96E-04	-1.51E-04	9.96E-04	-1.51E-04
	3.15E-03	-4.87E-04	3.15E-03	-4.87E-04	3.15E-03	-4.87E-04	3.15E-03	-4.87E-04	3.15E-03	-4.79E-04	3.15E-03	-4.79E-04	3.15E-03	-4.79E-04	3.15E-03	-4.79E-04
	9.95E-03	-1.54E-03	9.95E-03	-1.54E-03	9.95E-03	-1.54E-03	9.95E-03	-1.54E-03	9.95E-03	-1.51E-03	9.95E-03	-1.51E-03	9.95E-03	-1.51E-03	9.95E-03	-1.51E-03
Best Fit Resistance [ohm]		-1.55E-01		-1.55E-01		-1.55E-01		-1.55E-01		-1.52E-01		-1.52E-01		-1.52E-01		-1.52E-01

2.7 Effect on the thermoreflectance of metals

The optical properties of metal films depend on fabrication process. To ensure good signal fidelity, the thermoreflectance change signals of the metal films on the same chip of the nano-patterned heater arrays are measured prior to the size-dependent measurement. Fig. S8 shows a large contrast in the signal amplitude measured from one sample.

To estimate how much the detected signal from a typical hybrid structure represents the surface temperature change (signal fidelity), the normalized thermoreflectance signal ($\Delta R/R$) is simulated using the RF module in the commercial software package: COMSOL Multiphysics. A linear temperature-dependent optical property of the metals is considered. Normalized thermoreflectance change signals ($\Delta R/R$) are obtained for metallic heaters and hybrid structures, respectively, and the signal fidelity is defined as their normalized ratios. The corresponding thermoreflectance change of aluminum and silver films are also simulated, and their ratio is denoted by $\Delta R_{Al} / \Delta R_{Ag}$. The simulation results as shown in Fig. S8c is used to estimate the signal fidelity.

11

To verify modeling results, we performed experiments on sapphire down to a 30 nm dot size (Figure S8d and Fig.2d in the main text). This figure includes the thermal conductivity extracted from pure Al dots, which does not have an issue related to the signals from two metals, and from the hybrid structure between them. The agreement between the thermal conductivity values measured using the two methods give confidence in the results obtained with the hybrid structure.
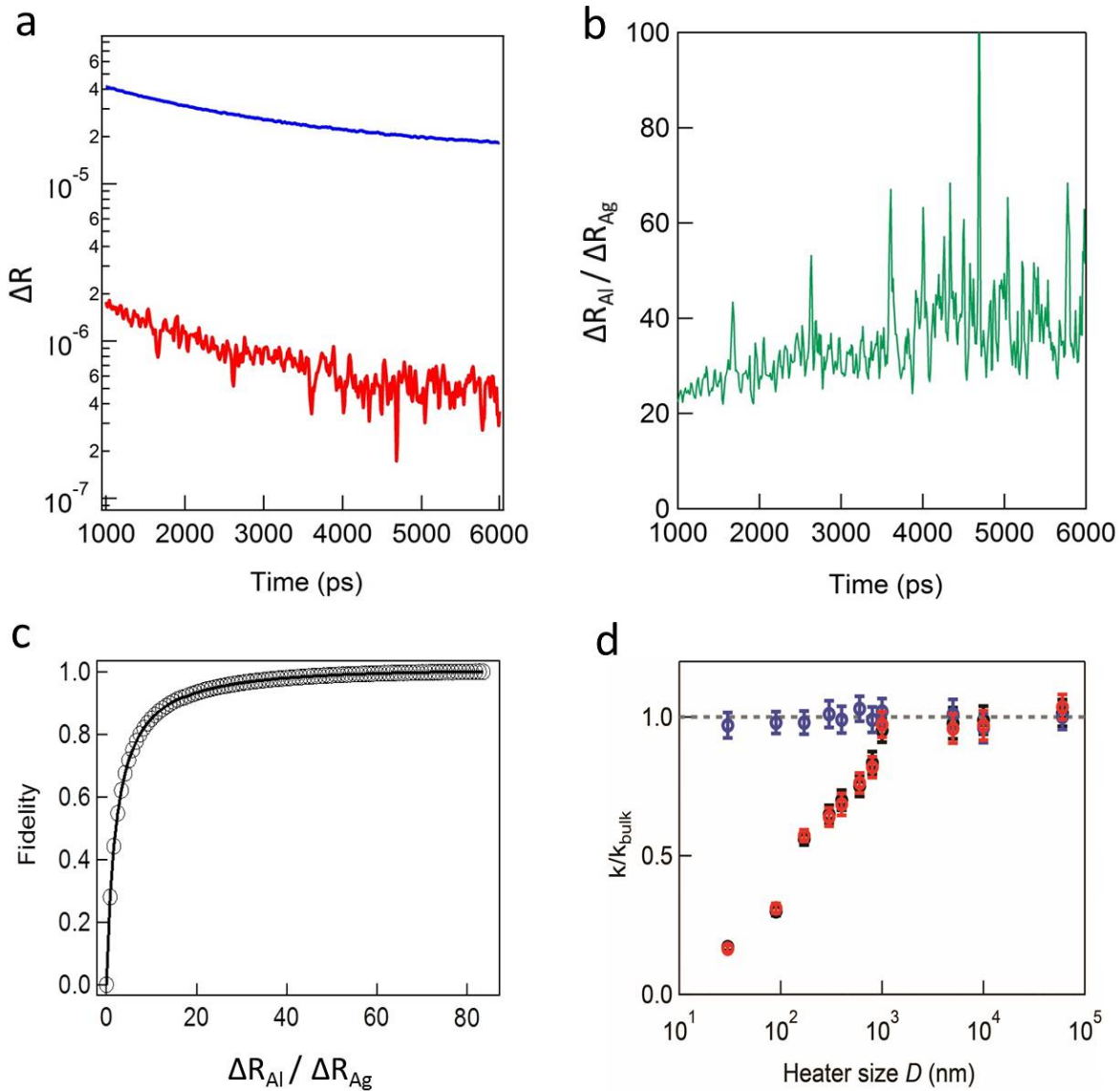
Supplementary Figure 8. a, Thermoreflectance change (ΔR) is measured by TDTR, for an aluminum film (blue) and silver film (red). **b,** the ratio of ΔR between aluminum and silver film plotted with time-dependence. **c,** simulated signal fidelity for a heater size $D = 170$ nm, as a function of the ratio ($\Delta R_{Al} / \Delta R_{Ag}$). **d,** experimental verification is performed using a transparent material -- sapphire (figure is re-plotted from Fig. 2d in the main text). Data measured from sapphire samples with pure aluminum heaters (red) and hybrid structures (black) show no appreciable difference in the thermal conductivity when using different heater sizes, within the measurement error range.

12

2.8 Surface acoustic waves (SAWs).

For most data points, no appreciable SAW signal is observed in the detected TDTR signal (as shown in Fig. 2c and Fig. S2). However, SAW signals are observed for samples with a heater size value $D = 400$ nm. For the data with SAWs (Fig. S9), the averaged signal is fit by the Fourier law to obtain thermal properties [13].
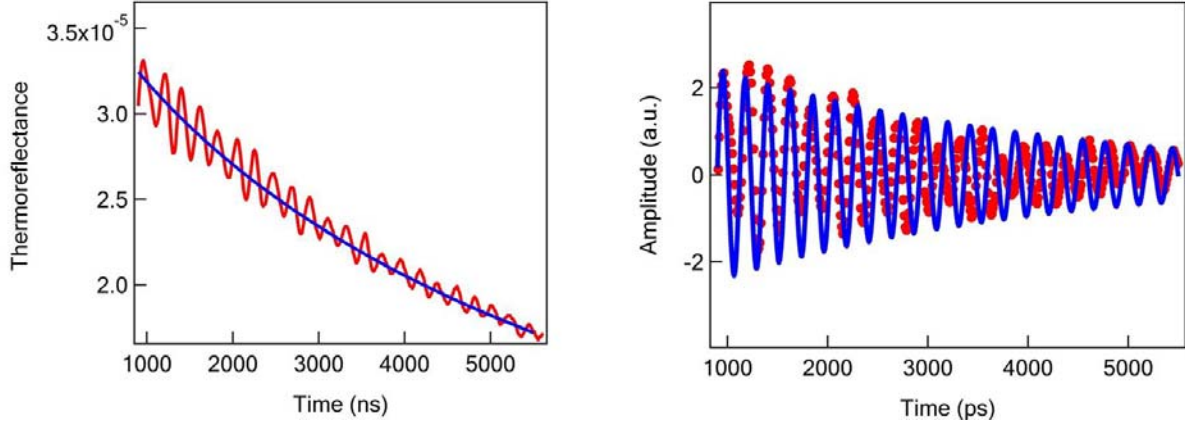
Supplementary Figure 9. SAW is appreciable when the heater size D = 400 nm, and the fitting is shown for (a) the thermal properties (blue line) and (b) the SAW lifetime.

2.9 Approximate expression for k_{eff} under the constant MFP assumption

The problem of ballistic electron transport at point contact was treated by Sharvin [14] and Wexler [15], and similar phenomenon can be expected for phonon transport [15-17]. It is worthwhile to see whether our experiment can be fitted with a simple expression assuming a constant MFP following a similar approach. We derive below an approximate expression under a constant MFP approximation. In the stead-state and purely ballistic limit, Wexler obtained the spreading resistance as (Eq.(11) in his paper)

$$R_{S,b} = \frac{8\Lambda}{3\pi k D^2} \tag{S8}$$

where D is the diameter of the constriction. In the diffusion limit, the spreading resistance is given by

$$R_{S,D} = \frac{1}{2Dk} \tag{S9}$$

13

One way to bridge the ballistic limit and the diffusion limit is to sum up the diffusion and ballistic resistances such that the effective thermal resistance is correct in both the purely ballistic and purely diffusive limits:

$$\frac{1}{2Dk_{eff}} = \frac{8\Lambda}{3\pi k_b D^2} + \frac{1}{2Dk_b} \tag{S10}$$

$$\frac{k_{eff}}{k_b} = \frac{1}{1 + \frac{16}{3\pi}\frac{\Lambda}{D}} \tag{S11}$$

where k_b is the bulk thermal conductivity. This expression is similar to other approximations that we often see in heat conduction and radiation, including the one that Chen gave before for heat conduction surrounding a nanoparticle [16]. In Fig. S10, we plotted k_{eff}/k_b vs. D/Λ, by optimizing the Λ values to achieve the best fit. One can see that using Eq. (S11), we can reasonably fit the experimentally determined k_{eff} by taking an average MFP value equaling to 935 nm. Despite the reasonable fitting, we should not undermine the fact that MFP varies widely as derived from our experiment. In fact, it has not been possible to determine this average MFP value without the measured effective k_{eff} data.
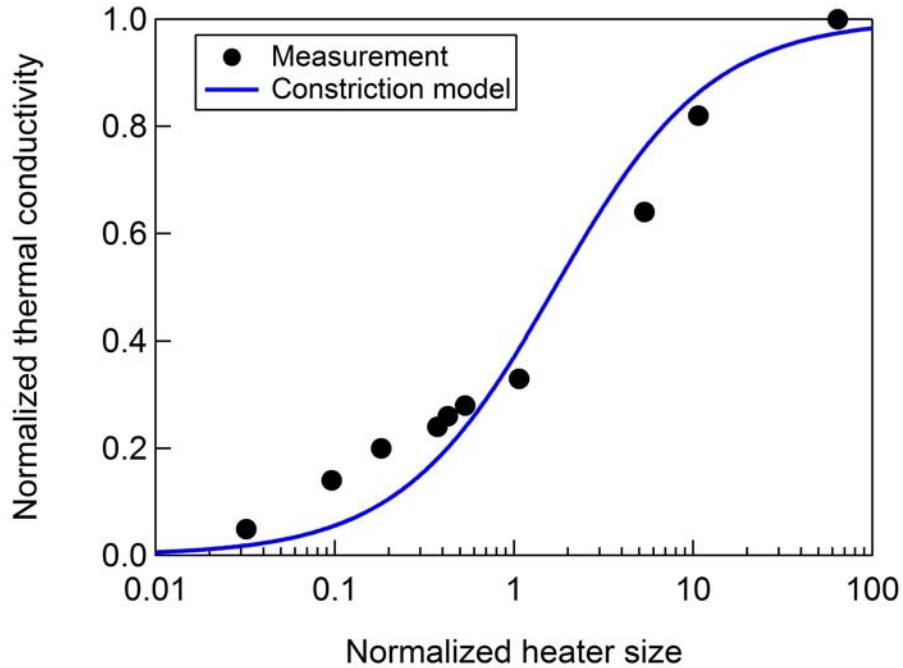
Supplementary Figure 10. Comparison between the measurement and prediction from the constriction resistance model.

14

References

[1] Cahill, D.G., Analysis of heat flow in layered structures for time-domain thermoreflectance, *Rev. Sci. Instrum.* 75, 5119 (2004).

[2] Carslaw, H. and Jaeger, J., Conduction of Heat in Solids (Oxford University Press, Oxford, 1959), 2nd ed.

[3] Peraud, J-P M., Hadjiconstantinou, N.G., Efficient simulation of multidimensional phonon transport using energy-based variance –reduced Monte Carlo formulations. *Phys. Rev. B* 84, 205331 (2011).

[4] Peraud, J-P M., Hadjiconstantinou, N.G., An alternative approach to efficient simulation of micro/nanoscale phonon transport. *Appl. Phys. Lett.* 101, 153144 (2012).

[5] Esfarjani, K., Chen, G., and Stokes, T., Heat transport in silicon from first-principles calculations, *Phys. Rev. B* 84, 085204 (2011).

[6] Minnich, A. J., Chen, G., Mansoor, S., and Yilbas, B.S., Quasiballistic heat transfer studied using the frequency-dependent Boltzmann transport equation, *Phys. Rev. B* 84, 235207 (2011).

[7] Hao, Q., Chen, G., and Jeng, M.S., Frequency-dependent Monte Carlo simulations of phonon transport in two-dimensional porous silicon with aligned pores, *J. Appl. Phys.* 106, 114321 (2009).

[8] Chen, G., Thermal conductivity and ballistic-phonon transport in the cross-plane direction of superlattices, *Phys. Rev. B* 57, 14958 (1998).

[9] Collins et al., Non-diffusive relaxation of a transient thermal grating analyzed with the Boltzmann transport equation, J. Appl. Phys. 114, 104302 (2013).

[10] Hu, Y., Kuemmeth, F., Lieber, C. and Marcus C. Hole spin relaxation in Ge-Si core/shell nanowire qubits. *Nature Nanotechnol.* 7, 47 (2012).

[11] Zeng, L. and Chen, G., Disparate quasiballistic heat conduction regimes from periodic heat sources on a substrate. *J. Appl. Phys.* 116, 064307 (2014).

[12] Wilson, R.B. and Cahill, D.G., Anisotropic failure of Fourier theory in time-domain thermoreflectance experiments, *Nature Comm.* 5, 5075 (2014).

[13] Cuffe, J. et al., Lifetimes of confined acoustic phonons in ultrathin silicon membranes, *Phys. Rev. Lett.* 110, 095503 (2013).

[14] Sharvin, Y.V., A possible method for studying Fermi surfaces. *Sov. Phys. JETP* 21, 655 (1965).

[15] Wexler, G., The size effect and the non-local Boltzmann transport equation in orifice and disk geometry, *Proc. Phys. Soc. London* 89, 927 (1966).

[16] Chen, G., Nonlocal and nonequilibrium heat conduction in the vicinity of nanoparticles, *J. Heat Transfer* 118, 539 (1996).

[17] Pettes, M.T. and Shi, L. A reexamination of phonon transport through a nanoscale point contact in vacuum, *J. Heat Transfer* 136, 032401 (2014).